The Astrophysical Journal, 881:128 (11pp), 2019 August 20 https://doi.org/10.3847/1538-4357/ab2b9c

Toward Rate Estimation for Transient Surveys. I. Assessing Transient Detectability and Volume Sensitivity for iPTF

Deep Chatterjee[1], Peter E. Nugent[2,3], Patrick R. Brady[1], Chris Cannella[4], David L. Kaplan[1], and Mansi M. Kasliwal[4]
[1] Department of Physics, University of Wisconsin, Milwaukee, WI 53201, USA
[2] Department of Astronomy, University of California, Berkeley, CA 94720-3411, USA
[3] Lawrence Berkeley National Laboratory, Berkeley, CA 94720, USA
[4] Cahill Centre for Astrophysics, California Institute of Technology, 1200 East California Boulevard, Pasadena, CA 91125, USA
Received 2019 May 15; revised 2019 June 18; accepted 2019 June 19; published 2019 August 21

Abstract

The past couple of decades have seen an emergence of transient detection facilities in various avenues of time-domain astronomy that have provided us with a rich data set of transients. The rates of these transients have implications in star formation, progenitor models, evolution channels, and cosmology measurements. The crucial component of any rate calculation is the detectability and spacetime volume sensitivity of a survey to a particular transient type as a function of many intrinsic and extrinsic parameters. Fully sampling that multidimensional parameter space is challenging. Instead, we present a scheme to assess the detectability of transients using supervised machine learning. The data product is a classifier that determines the detection likelihood of sources resulting from an image subtraction pipeline associated with time-domain survey telescopes, taking into consideration the intrinsic properties of the transients and the observing conditions. We apply our method to assess the spacetime volume sensitivity of type Ia supernovae (SNe Ia) in the intermediate Palomar Transient Factory (iPTF) and obtain the result, $\langle VT\rangle_{\rm Ia} = (2.93 \pm 0.21) \times 10^{-2}\,{\rm Gpc}^3\,{\rm yr}$. With rate estimates in the literature, this volume sensitivity gives a count of 680–1160 SNe Ia detectable by iPTF, which is consistent with the archival data. With a view toward wider applicability of this technique we do a preliminary computation for long-duration type IIp supernovae (SNe IIp) and find $\langle VT\rangle_{\rm IIp} = (7.80 \pm 0.76) \times 10^{-4}\,{\rm Gpc}^3\,{\rm yr}$. This classifier can be used for computationally fast spacetime volume sensitivity calculation of any generic transient type using their light-curve properties. Hence, it can be used as a tool to facilitate calculation of transient rates in a range of time-domain surveys, given suitable training sets.

Key words: Supernovae – Transient detection – Type Ia supernovae – Type II supernovae

1. Introduction

The past two decades have brought about a revolution in the field of time-domain optical astronomy with experiments like the Sloan Digital Sky Survey (Sako et al. 2007), the Palomar and intermediate Transient Factory (PTF; Law et al. 2009), the Catalina survey (Drake et al. 2009), Pan-STARRS (Kaiser et al. 2010), the ATLAS survey (Shanks et al. 2015), Zwicky Transient Facility (ZTF; Kulkarni 2016), and the All-Sky Automated Survey for Supernovae (Holoien et al. 2019) performing all-sky searches with a rolling cadence to locate transients. The timescale of these transients varies from a few minutes, like M dwarf flares, up to a few weeks or months, like supernovae.

Studying transient rates is essential to understanding the progenitor systems and environments they occur in. For example, while core-collapse supernovae are associated with more recent massive stars, SNe Ia occur in both younger and older populations (Maoz & Mannucci 2012). The distribution of transients in space and time helps us understand metal enrichment, galaxy formation, and the overall evolution of the universe. The classification and compilation of transients from the surveys provide a rich data set that can be used to make statements about their rates and population. Next-generation surveys like the Large Synoptic Survey Telescope (Ivezić et al. 2008) are expected to make significant additions to already existing catalogs with wide–deep–fast searches.

A quantitative assessment of the transient detectability by the survey is an essential component required to study transient rates. A survey could miss the observation and confirmation of transients for reasons of being intrinsically dim, occurring when the instrument was not observing, poor weather conditions, and so on. Therefore, it is crucial to understand the circumstances under which the survey is sensitive in recovering transients. The transient detectability leads to the calculation of a spacetime sensitive volume to particular transient types. This depends on properties of the source and its environment, like its brightness or its host galaxy brightness. The instrument cadence and observing schedule are also expected to contribute significantly. A fast cadence is necessary to capture the evolution of, say, an M dwarf flare, which last a few minutes, as opposed to a supernova, which evolves for a couple of months.

We consider the intermediate Palomar Transient Factory (iPTF), the successor of PTF, and the predecessor of ZTF. As a first step, we assess the efficiency of the real-time image subtraction pipeline. We insert fake transients with varying properties into the original iPTF images and then run the pipeline to test recovery. This forms our *single-epoch* detectability. While this step is similar to the work done for the PTF pipeline by Frohmaier et al. (2017), our analysis differs in final data product for the single-epoch detectability. We make use of supervised machine learning to train a classifier on missed and found fake transients reported by the pipeline to make predictions about the detectability of an arbitrary transient. For completeness, we note that the performance of the survey in the galactic plane is expected to be different from the high-latitude fields and requires a separate analysis. The

analysis presented in this paper could be applied to only galactic fields to obtain the detection efficiency in the galactic plane. Here, we study the detectability in the high-latitude fields or, alternatively, of transients of extragalactic origin. Under such a consideration, this step is independent of the transient type. The multiepoch observation and detection of a transient can be done using the single-epoch detectability at each epoch. The use of machine learning in this case has advantages in the areas of computing time, determination of systematic errors, ease of improving accuracy at the cost of computing time when required, and handling correlation between training parameters. As a second step, we consider the transient light-curve evolution. We simulate transient light curves in spacetime and use the iPTF observing schedule in conjunction with this classifier to get the epochs at which the transient is detected. We restrict to type Ia and type IIp supernova light curves in this work, the former being the primary result. For the type Ia supernovae (SNe Ia), we impose a minimum number of five epochs of detection brighter than 20th magnitude with at least two during the rise and at least two during the fall of the light curve to be a "confirmed" SN Ia. The simulated SNe Ia are used to do a Monte Carlo integral over spacetime to obtain the spacetime volume sensitivity. For the type IIp supernovae (SNe IIp) light curves, the procedure is the same, except we consider a IIp light curve recovered if there are at least five epoch observations brighter than 20th magnitude within a span of three weeks during the "plateau" phase.

The organization of the paper is as follows. In Section 2 we give a brief description of the iPTF real-time image subtraction pipeline. In Section 3 we give details of the procedure of injecting fake transients into original iPTF images. We present the results after running the image subtraction pipeline in Section 4. Here, we select a subset of parameters that captures maximum variability in detecting transients, train a classifier based on the missed and found fake transients, and cross-validate the performance of the classifier. In Section 5 we use an SN Ia light-curve model to simulate an ensemble of transients uniform in comoving volume, pass them through the four-year observing schedule, and determine the fraction that would be detectable by iPTF. This is then used to compute the spacetime volume sensitivity for SNe Ia. A similar but simpler analysis is also done for SNe IIp to obtain its spacetime sensitive volume. Finally, in Section 6 we present the procedure of getting the rate posterior assuming the detections to be a Poisson process with a mean intrinsic rate.

2. Intermediate Palomar Transient Factory

The iPTF was a survey operated at the Palomar Observatory between late 2012 and early 2017. It had two filters: R (centered at 6581 Å) and g (centered at 4754 Å). It performed fast-cadence experiments resulting in about 300–400 exposures on a good night with a nightly output of about 50–70 GB. The images were processed by the real-time image subtraction pipeline to report transients within minutes latency. Details are presented in Nugent et al. (2015) and Cao et al. (2016). Here, we give a brief description.

2.1. iPTF Image Subtraction Pipeline

The iPTF real-time image subtraction pipeline (henceforth ISP) was hosted at the National Energy Research Scientific Computing Center (NERSC). A complete exposure of 11 working CCDs was transferred to NERSC immediately after data acquisition to search for new candidates. The pipeline preprocessed the images to remove bias and correct for flat-fielding. It solved for astrometry and photometry, and performed image subtraction using the `HOTPANTS` algorithm (Becker 2015). New candidates were assigned a *real–bogus* classification score between 0 and 1 corresponding to bogus and real, respectively (Bloom et al. 2013). Additionally, candidates would be cross-matched to external catalogs to remove asteroids, active galactic nuclei, and variable stars.

3. Fake Transients

In order to quantify the performance of the iPTF ISP, we perform an end-to-end simulation using fake transients. We inject fake point-source transients in the iPTF images and then run the pipeline on both the original images and the faked ones. The transients are either missed or found by the ISP, which forms the detectability. We find the efficiency by binning up the parameter space and taking the ratio of found to total transients in them. Regarding the mnemonic in subsequent sections, we make a distinction between the terms *detectability* and *efficiency*. Detectability is a decision taken in the sense of a yes/no, while efficiency is the ratio mentioned above. The former is a binary decision, either of $\{0, 1\}$, while the latter is a quantity $\in[0, 1]$.

3.1. Point-source Transients

We follow the *clone stamping* technique used by Frohmaier et al. (2017) for PTF to perform our fake point-source injections. The parameters describing these fake transients are *single epoch*—they represent the intrinsic properties of the object and observing conditions at a particular epoch. In other words, here we assess the detectability given the transient was in the field of view of the instrument.

The computational cost for performing injections into all iPTF images and running ISP on them is significant. Therefore, we carry out the process in a single iPTF field 100019. We choose this field since the distribution of the transient population in this field is an accurate representation of the transient population in the sky observed from Palomar (see Figure 1 of Frohmaier et al. 2017).

The fake injections are *bright* stars chosen from each original image. These are objects having the following properties:

$$\begin{aligned} m_* &\in [13.5, 16]; \quad \texttt{CLASS\_STAR} \in [0.5, 1.0] \\ \texttt{FWHM} &\in [1.0, 3.0]; \quad \texttt{ELLIP} \in [0.0, 0.3]. \end{aligned} \tag{1}$$

Here m_* is the apparent magnitude, and `CLASS_STAR` is a quantity having a value between 0 (not star-like) and 1 (star like). `FWHM` is the full width at half maximum, in pixels. `ELLIP` is the ellipticity of the object. These quantities are reported after running `SExtractor` (Bertin & Arnouts 1996) on the original images. The reason we choose objects in this range is because we want the point-spread function (PSF) to be well estimated, which is the case for bright stars having a high signal-to-noise ratio $\gtrsim$100 ($m_* \leqslant 16$). At the same time we want to avoid pixel saturation and therefore select stars with $m_* \geqslant 13.5$. Objects falling in a 50 pixel wide edge boundary

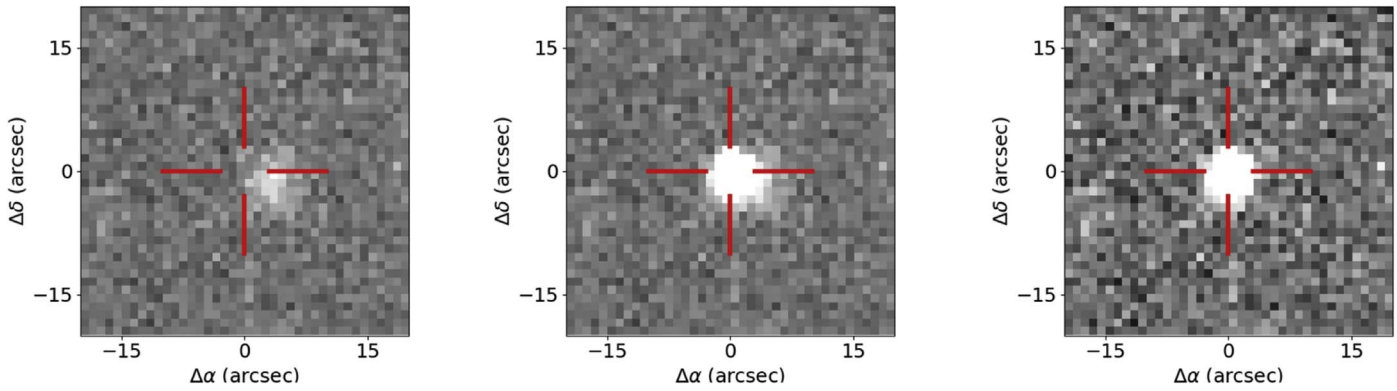

(a) Brighter fake transient

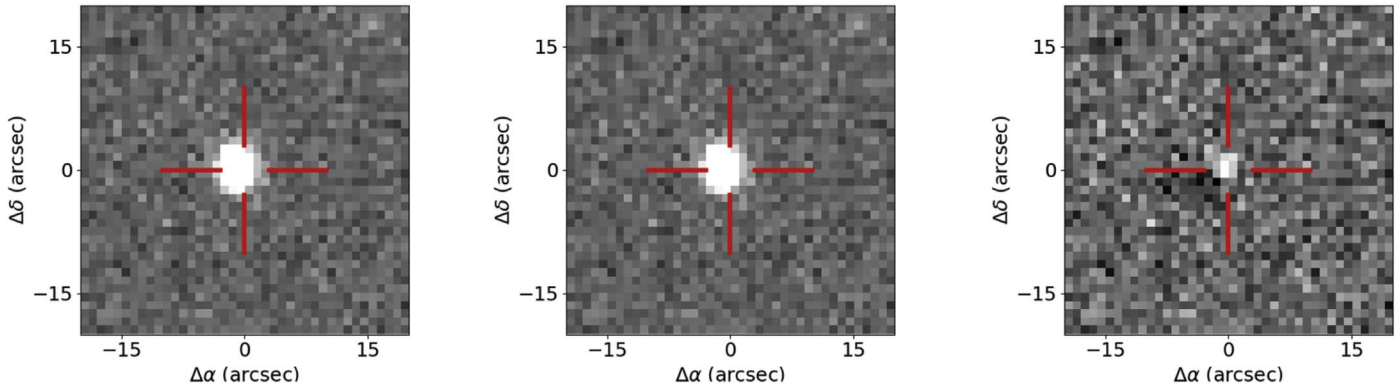

(b) Dimmer fake transient

Figure 1. Example of an injected transient and the corresponding difference image thumbnail obtained after the image subtraction. The leftmost thumbnail (both panels) is from the original image, the middle thumbnail is a result after a transient is injected, and the right thumbnail shows the difference image. The location of the crosshair is the approximate point where the transient was injected.

are left out since they could potentially be affected by image subtraction artifacts.

A square of side length $\sim 9''$,[5] centered around the star and local-background subtracted, constitutes a *stamp*. A stamp containing any other object apart from the source star is avoided. The local background refers to that reported by `SExtractor`. The stamp is scaled by an appropriate scaling factor to create a point-source transient of desired magnitude. Each transient is allocated a host galaxy.[6] We follow Frohmaier et al. (2017) regarding the location in the host and place our stamp at a random pixel location within an elliptical radius[7] of 3 pixels. This value contains a sufficient amount of the flux from the galaxy.

This procedure is performed on all the images in field 100019 of iPTF, 10-fold, with a total of $\approx 2.24 \times 10^6$ injected transients. The transient magnitudes are chosen uniformly between the 15th and 22nd magnitudes with the constraint that the stamp is one magnitude fainter than the original star. We only rescale to fainter magnitudes because we do not want artifacts like noise residuals from the average background subtraction to be scaled up as noise spikes. Therefore, $m_{\rm inj}$ is as follows:

$$m_{\rm inj} \sim \begin{cases} U(15, 22); & m_* \in (13.5, 14) \\ U(m_* + 1, 22); & \text{otherwise} \end{cases}. \quad (2)$$

An example of an injected transient in a galaxy and the new object recovered by the ISP is shown in Figure 1.

3.2. Recovery Criteria

The recovery efficiency ε is defined as the ratio of the number of injections recovered in a part of the parameter space to the total number of injections in that part. Let our injections be described by parameters $\boldsymbol{\lambda}$, then

$$\varepsilon(\boldsymbol{\lambda}) = \frac{N_{\rm rec}(\boldsymbol{\lambda}) d\boldsymbol{\lambda}}{N_{\rm tot}(\boldsymbol{\lambda}) d\boldsymbol{\lambda}}. \quad (3)$$

The quantities in the numerator and denominator are the number of recovered and total injections, respectively, $\in(\boldsymbol{\lambda}, \boldsymbol{\lambda} + d\boldsymbol{\lambda})$. Here $\boldsymbol{\lambda}$ includes both intrinsic source properties of the transient and its environment along with the observing conditions. Examples of intrinsic properties include the magnitude of the transient and the surface brightness of the

[5] More precisely, 9 pixels. 1 pix. $\approx 1\farcs01$.

[6] About 50 fake transients were injected in each image; 90% having an associated host galaxy, 10% away from any host galaxy. In this study we only use the injections in host galaxies.

[7] `KRON_RADIUS` in `SExtractor`.

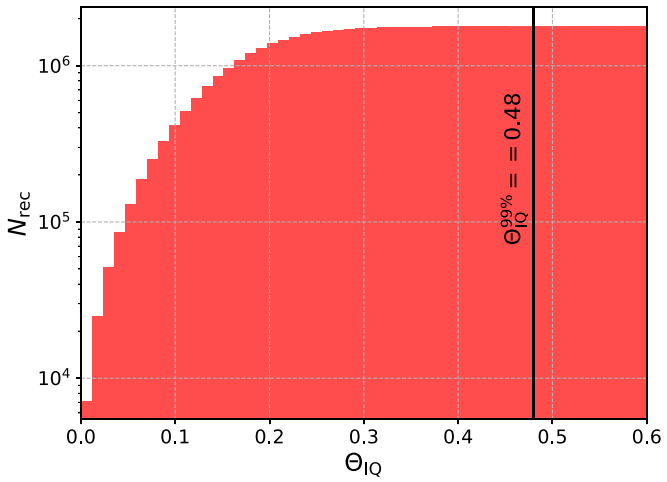

Figure 2. Cumulative histogram of the quantity Θ_{IQ}, defined as the ratio between the astronomical seeing of the image to that of the reference image as given in Equation (4). The threshold value $\Theta_{IQ}^{99\%} = 0.48$ corresponds to the 99th percentile. We place a constraint of this value when the objects recovered by the pipeline are spatially cross-matched to an injected transient.

host galaxy, whereas those for observing conditions include airmass or sky brightness. While we control fake transient brightness, the observing conditions are those of the images themselves. Since images across the full survey time are used, the parameter space of the observing conditions is automatically spanned.

We determine recovery based on the spatial cross-matching of the injections with new objects reported after running the ISP. To determine the tolerance to be imposed during the cross-matching, we define Θ_{IQ} as

$$\Theta_{IQ} = \frac{\sqrt{(x_{inj} - x_{rec})^2 + (y_{inj} - y_{rec})^2}}{\Phi}, \quad (4)$$

where Θ_{IQ} is the distance between the injected and the recovered sources in units of the seeing, Φ.

We choose the threshold of Θ_{IQ} such that 99% of the found injections lie within this threshold, which has a value of $\Theta_{IQ}^{99\%} = 0.48$ (see Figure 2). We also impose a real–bogus score threshold `RB2` $\geqslant 0.1$ on the new object. This threshold on `RB2` is inspired from survey operation thresholds. Out of the $\approx 2.24 \times 10^6$ injections, we recover $\approx 1.62 \times 10^6$.

4. Single-epoch Detectability

In this section we discuss the results of the injection campaign mentioned in Section 3. We first show some of the *single-parameter* efficiencies as a comparison with those obtained for PTF (see Figure 5 of Frohmaier et al. 2017). For the joint multidimensional detectability, our analysis differs from Frohmaier et al. (2017). We treat the problem of detecting a transient in a single epoch as a *binary classification* problem and use the machinery of supervised learning to predict whether a transient is detected in that epoch.

4.1. Single-parameter Efficiencies

The *single-parameter* efficiency is the marginalized version of Equation (3). Suppose our parameter of interest is θ and the other "nuisance" parameters are given by γ, such that in Equation (3), $\boldsymbol{\lambda} = \{\theta, \gamma\}$. The single-parameter efficiency is

$$\varepsilon(\theta) = \frac{\left[\int_\gamma N_{rec}(\theta, \gamma) d\gamma\right] d\theta}{\left[\int_\gamma N_{tot}(\theta, \gamma) d\gamma\right] d\theta}. \quad (5)$$

In Figure 3 we show the single-parameter efficiencies. The expected trend of missing faint transients is seen in the plot for m_{inj}. We find that the recovery efficiency starts to drop for transients by the 20th magnitude and sensitivity is almost nil by the 22nd magnitude.

4.2. Multidimensional Detectability

In this section, we make a selection of parameters from the full parameter set, $\boldsymbol{\lambda}$, to those on which the detectability depends strongly. In other words, the detectability is a multivariate function of all the possible parameters that influence the detection of a transient. We identify the minimal set that captures maximum variability. There can be correlations among a pair of parameters. For example, the sky brightness, F_{sky}, and the limiting magnitude, m_{lim}, are correlated—a bright sky hinders the depth and results in a low value of limiting magnitude. The variation of the marginalized efficiencies shown in Figure 3 assist us with the choice of such a parameter set. Since the trend in the single-parameter efficiencies are similar to those from PTF, we select the parameters considered by Frohmaier et al. (2017) with a minor difference in the usage of the galaxy surface brightness directly, as used in Frohmaier et al. (2018), in place of the F_{box}[8] parameter used in the former. This is justified because our fakes were injected in galaxies.

We choose, the following set to represent the dependence of detectability:

$$\boldsymbol{\beta} = \{m, S_{gal}, F_{sky}, \Phi_{IQ}, m_{lim}\}. \quad (6)$$

Here m is the apparent magnitude of the transient, S_{gal} is the host galaxy surface brightness, F_{sky} is the sky brightness, Φ_{IQ} is the ratio of the astronomical seeing to that of the reference image, and m_{lim} is the limiting magnitude. The quantities m and S_{gal} are natural in capturing detectability. Sky brightness affects the detectability in a strong way, as is apparent from Figure 3. The Φ_{IQ} parameter captures the variability of the atmosphere. Finally, the limiting magnitude, m_{lim}, although correlated with F_{sky}, captures longer exposure times and the status of instrument electronics.

With this set, we use the machinery of supervised learning provided by the `scikit-learn` library (Pedregosa et al. 2011) to train a binary classifier based on the results of the ISP. Once trained, the classifier outputs a probability of detection given arbitrary but physical values of $\boldsymbol{\beta}$. We denote this trained classifier by $\hat{\varepsilon}$:

$$\hat{\varepsilon} = \hat{\varepsilon}(m, S_{gal}, F_{sky}, \Phi_{IQ}, m_{lim}). \quad (7)$$

The `scikit-learn` library provides a suite of classifiers. We choose the nonparametric `KNearestNeighbor` classifier based on speed and accuracy given our large volume of training data. Our complete data set comprises $\sim 2.24 \times 10^6$ fake point-source injections of which $\sim 1.62 \times 10^6$

[8] Background-subtracted flux in a 3 ×3 box in the location of transient.

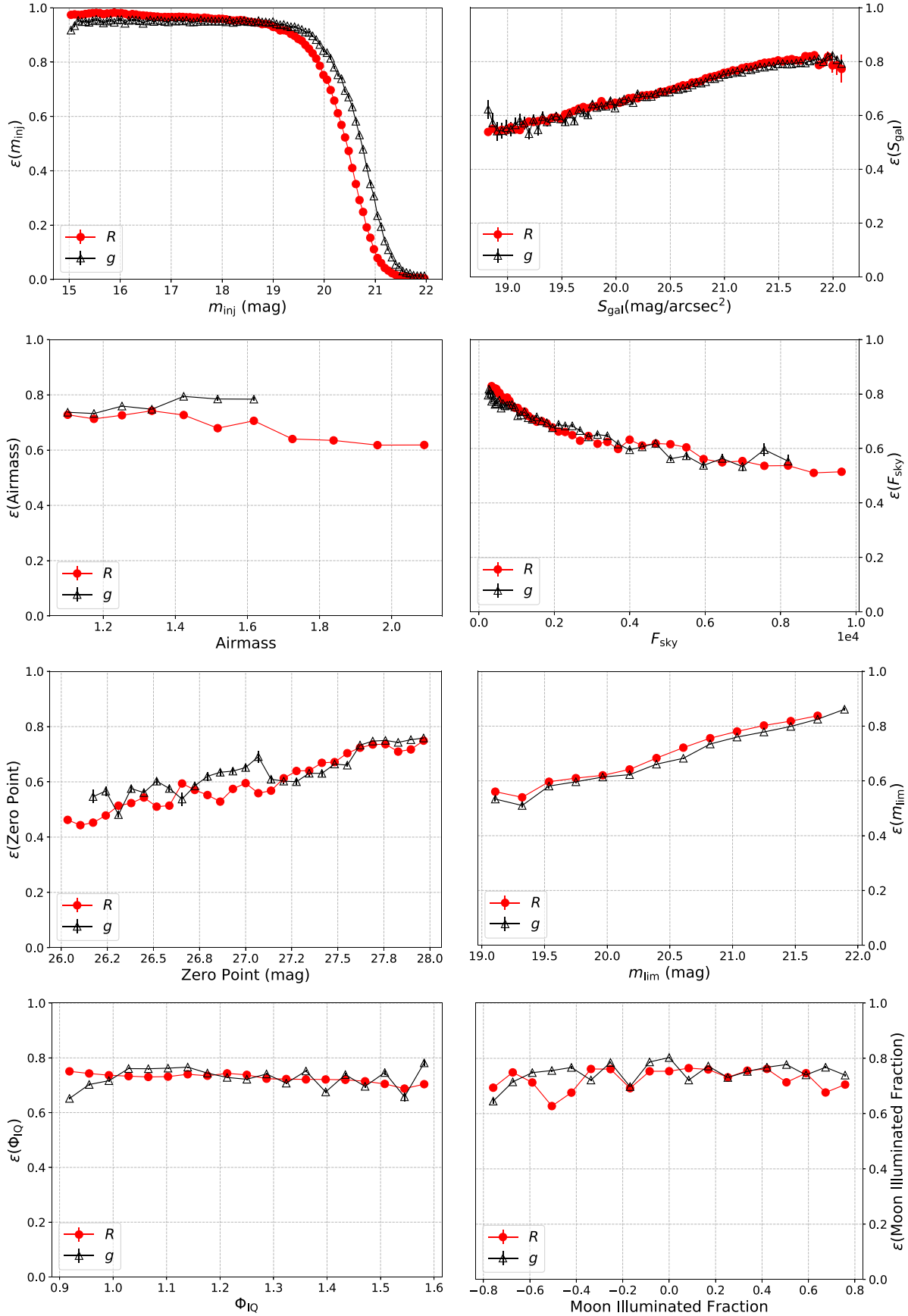

Figure 3. Single-parameter efficiencies, defined in Equation (5) are shown here. In each of the panels, the x-axis is the parameter of interest. The top two panels are parameters that are the intrinsic properties, while the remaining are those taken from observing conditions. We also separate out the efficiencies based on the filter. While small deviations exist in the curves the general trend is unchanged based on the filter. Since there was a greater number of images (almost 3 times for field 100019) taken in the R filter than the g filter during the iPTF survey, the range of observing conditions is larger for the R filter.

Table 1
Average Misclassification Obtained for the `KNearestNeighbor` Classifier

Training %	Testing %	Avg. Misclassification
75%	25%	5.776%
80%	20%	5.760%
85%	15%	5.745%
90%	10%	5.758%

Note. The complete data set contains $\approx 2.24 \times 10^6$ fake point-source injections of which $\approx 1.62 \times 10^6$ ($\approx 6.2 \times 10^5$) are found (missed) by the ISP. This is split into respective training and testing fractions. The right-most column shows the fraction of the testing set for which the predictions made by the classifier trained on the corresponding training fraction differed from the actual value. The misclassification does not change significantly as the size of training data is varied and is attributed mostly to systematics. We quote a conservative value of 6% as the systematic uncertainty of the classifier.

($\sim 6.2 \times 10^5$) are found (missed) by the ISP. We train the classifier using 11 neighbors—twice the number of dimensions plus one to break ties. The observation of a fiducial transient is a point in this parameter space. To decide if that point is "missed" or "found," we use a majority vote from the nearest 11 neighbors. To cross-validate the performance, the data set is split into a training set containing 90% of the full data set, and a testing set containing the remaining 10%. We checked that increasing the number of neighbors does not significantly increase the correctness of predictions made by the classifier. We note that one could use a different threshold for this classification. For example, a different option could be to use more than three "found" neighbors to call the arbitrary point as found. However, it comes at a cost of misclassification. From the predictions of the classifier on the testing set, we find the systematic uncertainty of the classifier to be $\approx$6% i.e., 6 out of 100 predictions made by the classifier are expected to be either true-negative or false-positive cases. The result does not change much if the size of the training and testing set is varied (see Table 1). A comparison between the predictions made by the trained classifier and the original ISP efficiency with the transient magnitude is presented in Figure 4. We see that the behavior of the ISP is reproduced by feeding the classifier with only a few thousand points randomly chosen from the parameter space.

5. Light-curve Recovery

In this section, we assess the detectability of light curves using SNe Ia as our case study. We simulate light curves with varying intrinsic properties, sky location, and redshift and use the single-epoch detectability classifier mentioned in Equation (7) together with the observing schedule of iPTF to determine their sensitivity. The steps are as follows:

1. We simulate light curves of varying intrinsic properties over spacetime.
2. From the complete iPTF observing schedule, we determine the observations of the evolving light curve. This depends on the duty cycle of the instrument. On extended periods with no observations, the simulated light curves are missed.
3. We associate a host galaxy with the supernova by choosing a surface brightness value from the distribution of galaxy surface brightness in the survey.

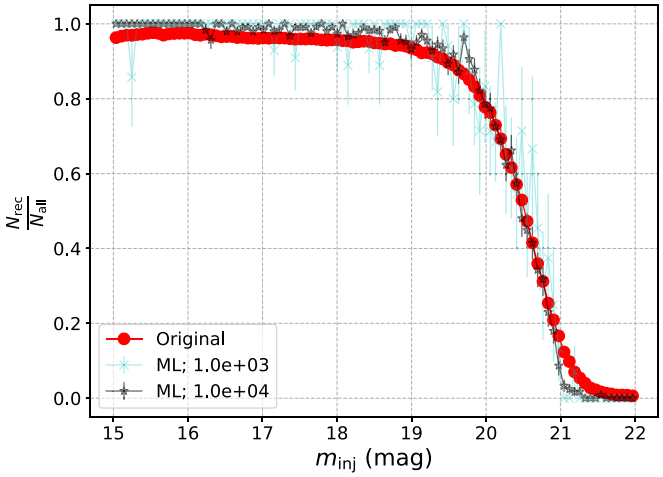

Figure 4. Comparison between single-parameter efficiency of transient brightness as predicted by the trained single-epoch classifier in Equation (7) vs. the distribution obtained from the ISP. The original curve has $\sim 10^6$ points used to train the classifier. The ML curves are made by binning the predictions made by the single-epoch classifier on a few thousand random points sampled from the parameter space of the injections (see Equation (6)). Two cases for 10^3 and 10^4 points are shown. We see that the behavior of the classifier converges to that of the ISP within a small sample size ($\lesssim$1% compared to the size of original distribution; see the Appendix for other parameters)

4. Every time the transient is "seen" by iPTF, we feed the combination of the apparent magnitude and host galaxy surface brightness along with the observing conditions at that epoch to the trained single-epoch classifier developed in Section 4. This step, in a sense, mimics the action of the ISP.
5. We call the light curve *recovered* when we have at least five found observations, all brighter than the 20th magnitude, with a minimum of two observations on the light-curve rise and a minimum of two on the fall. This is motivated by survey time discoveries.

We also consider SN II light curves for comparison. SNe II are complex and are further categorized into different subtypes. We consider the IIp subtype because compared to the $\sim$weeks-long variability of SNe Ia, IIp light curves vary $\sim$100 days and hence is a complementary case to study. The analysis for the IIps, however, is simpler compared to Ias.

5.1. SN Ia Light Curves

We use SN Ia light curves from the SALT2 model (Guy et al. 2007). In particular, we use the `Python` implementation of SALT2 provided in the `sncosmo` library (Barbary 2014). This model is based on observations of SNe Ia by the SDSS and SNLS surveys. The free parameters of the model include the stretch (x_1) and color (C) parameters of the SN Ia. Regarding the range of these parameters, we follow the same range as Frohmaier et al. (2017, see Table 1 and Equation (4) therein). The ranges cover the possible light-curve morphologies of SNe Ia (Betoule et al. 2014). We show an example light curve, at a redshift of $z = 0.01$ with an intrinsic $M_B = -19.05$ in Figure 5. When propagating the flux, we also take into account the extinction due to host galaxy dust and the Milky Way (MW) dust. We use the MW dust map by Fitzpatrick (1999), which is a part of the `sncosmo` package. For the host galaxy extinction, we use the distribution of $E(B-V)$ of SN Ia in their host galaxies (Hatano et al. 1998). Dust extinction plays

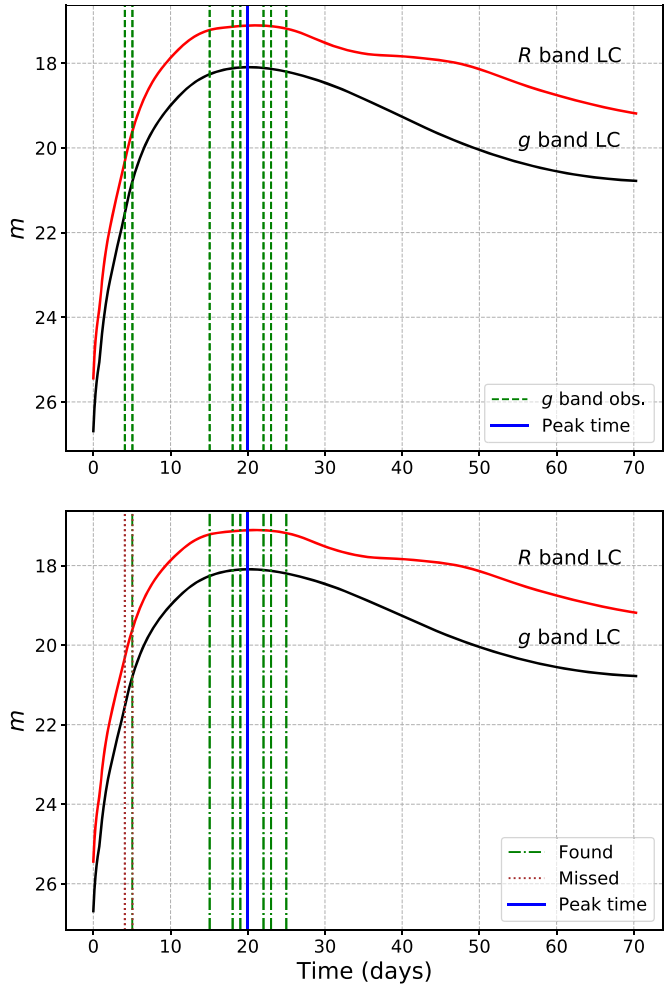

Figure 5. Upper panel: an example of a SALT2 light curve, with the apparent magnitude, m, on the y-axis and time on the x-axis. The light curves in the iPTF R and g bands are shown. The observations of the telescope are shown as vertical lines. At each observation, we also have the observing conditions of the telescope from archival data. Lower panel: the same light curve is plotted, however, the vertical lines now represent the detectability from the single-epoch classifier. Based on the criteria of confirming a light curve as SN Ia, this light curve was recovered.

a significant role in the detectability of light curves as the SNe can be dimmed by as much as 1–1.5 mag.

5.2. Light-curve Ensemble

We simulate $\approx 5 \times 10^6$ SN Ia light curves uniformly in a comoving volume up to a redshift, $z_{\rm max}^{\rm Ia} = 0.28$,[9] uniform in peak time distribution in the observer frame. We assume a flat ΛCDM cosmology with Hubble constant $H_0 = 69.3\,{\rm km\,s^{-1}\,Mpc^{-1}}$ and matter to critical density $\Omega_{\rm m} = 0.287$ (Hinshaw et al. 2013).[10] We associate a host galaxy surface brightness to each of these SNe using the distribution of surface brightness from iPTF data.

The epochs when the SN Ia is observed come from the iPTF observing schedule. At each observation, we obtain the transient magnitude at that epoch from the light curve and the observing conditions from the iPTF survey database. The single-epoch classifier then tells us the epochs when the transient was detected. An example is shown in Figure 5 where the vertical lines in the upper and lower panels, respectively, represent the observations and detections at each epoch.

5.3. SN Ia Spacetime Sensitive Volume

To understand rates, one must have a good estimate of the survey sensitivity to particular transient types. Let $\Lambda_{\rm SNe}$ be the expected count of SNe seen during survey time. Then, with R as the intrinsic rate we have

$$\begin{aligned}\Lambda_{\rm SNe} &= \int f(t; \underbrace{M_B, z, ...}_{\boldsymbol{\kappa}}) \overbrace{\frac{dN}{dt_e dV_c}}^{R} \frac{1}{1+z}\frac{dV_c}{dz} dz dt d\boldsymbol{\kappa} \\ &= R \int f(t; \underbrace{M_B, z, ...}_{\boldsymbol{\kappa}}) \frac{1}{1+z}\frac{dV_c}{dz} dz dt d\boldsymbol{\kappa} \\ &= R \langle VT \rangle, \end{aligned} \tag{8}$$

where the integral runs over time of observation and comoving volume up to $z_{\rm max}^{\rm Ia} = 0.28$. The *selection* function, $f(...) \in \{0, 1\}$, is to be interpreted as the weight assigned to regions in spacetime. The value of the selection function is a consequence of running a particular instance of SN Ia through the observing schedule and inferring detectability based on the single-epoch classifier in Equation (7). Therefore, the selection function depends on the observer time, t, which captures the duty cycle and cadence. Also, it depends on the intrinsic properties of the supernova like the absolute intrinsic magnitude, M_B, the redshift, z, at which it was simulated, the sky location, and so on. These are collectively represented by $\boldsymbol{\kappa}$ in Equation (8). Since we have distributed the supernovae uniformly in comoving volume, the integral is approximated in the Monte Carlo sense:

$$\begin{aligned}\langle VT \rangle &= \int f(t; \underbrace{M_B, z, ...}_{\boldsymbol{\kappa}}) \frac{1}{1+z}\frac{dV_c}{dz} dz dt d\boldsymbol{\kappa} \\ &\approx \frac{N_{\rm rec}}{N_{\rm tot}} T \int \frac{1}{1+z}\frac{dV_c}{dz} dz, \end{aligned} \tag{9}$$

where $N_{\rm rec}$ is the number of SNe recovered from this simulation campaign, $N_{\rm tot}$ is the total number simulated, and T is the four-year period of iPTF over which we performed the simulations.[11] We obtain the result

$$\langle VT \rangle_{\rm Ia} = (2.93 \pm 0.21) \times 10^{-2}\,{\rm Gpc^3\,yr}, \tag{10}$$

where the error includes the $\sim 1/\sqrt{N}$ statistical error from Monte Carlo integration and the 6% systematic error of the single-epoch detectability classifier computed in Section 4.2, the latter being the dominant source of error. The distribution of the detected SNe Ia in sky is shown in Figure 6 colored by redshift. Using the recovered SNe Ia, the median sensitive comoving volume is found to be $0.305\,{\rm Gpc^3}$. We report the redshift corresponding to this value as the median sensitive redshift to SNe Ia, $z_{\rm median}^{\rm Ia} = 0.099$, shown in Figure 7.

[9] The $z_{\rm max}^{\rm Ia} = 0.28$ is high enough to capture the spacetime boundary of iPTF sensitivity. Also, no simulations are done below a declination $\delta_{\rm min} \approx -31°$ consistent with hardware limitations for iPTF.

[10] `astropy.cosmology.WMAP9`.

[11] More specifically, 2012 October 23 to 2017 March 3 ⇒1592 days.

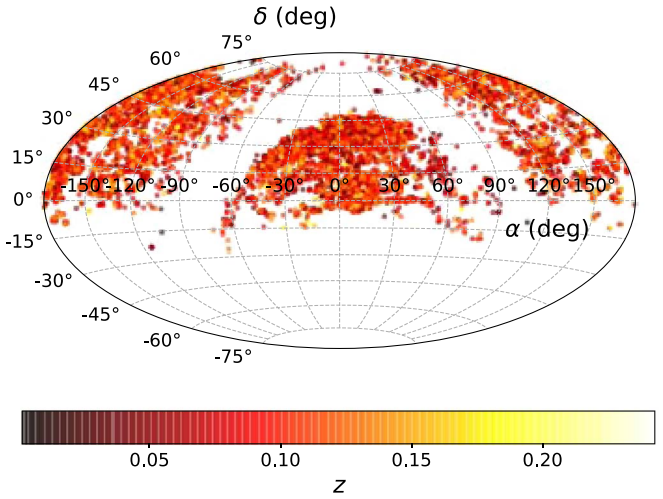

Figure 6. An ensemble of SN Ia light curves were simulated out to a redshift, $z_{\rm max}^{\rm Ia} = 0.28$, uniform in comoving volume. This figure shows the distribution of the recovered SN Ia in the sky colored by the redshift. The galactic plane can be seen as the half-annulus region with no detections.

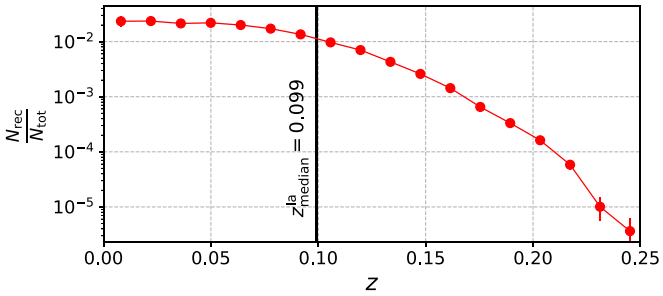

Figure 7. Recovery efficiency of the SN Ia light curves as a function of redshift, z. The median volume-weighted redshift is found to be $z_{\rm median}^{\rm Ia} = 0.099$.

5.4. SN IIp Spacetime Sensitive Volume

In contrast to the well-defined Ia light curves with their typical timescales of several weeks, we also wanted to explore longer-timescale light curves as a limiting case. Therefore, we consider SNe IIp and compute their spacetime sensitive volume in similar lines as Section 5.2. In general, type II supernovae (SNe II) vary in light-curve morphology and are categorized in various subtypes (Li et al. 2011). Specifically, type IIp light curves have a distinct "plateau" feature after the rise lasting for about 100 days after explosion, as shown in Figure 8. The intrinsic brightness, $M_B \sim -16.75$, is significantly lower than that of SNe Ia (Richardson et al. 2014). Hence, we expect the spacetime sensitive volume to be lower than that of the SNe Ia. When considering the Ia light curves in Section 5.1, the SALT2 model parameters were used to tune possible light-curve morphologies. Here we take a simpler approach and consider a time-series model from Gilliland et al. (1999; named `nugent-sn2p` in the `sncosmo` package) to compute the flux up to 100 days from the explosion time. Thus, while simulating the SNe IIp in spacetime, the only change to the light-curve shape is the "stretch" depending on the cosmological redshift.

We simulate $\sim 9.1 \times 10^5$ SN IIp light curves uniform in sky location, observer time, and comoving volume up to a redshift $z = 0.1$. Like the SNe Ia, each SN IIp is assigned a host galaxy surface brightness from the surface brightness distribution of

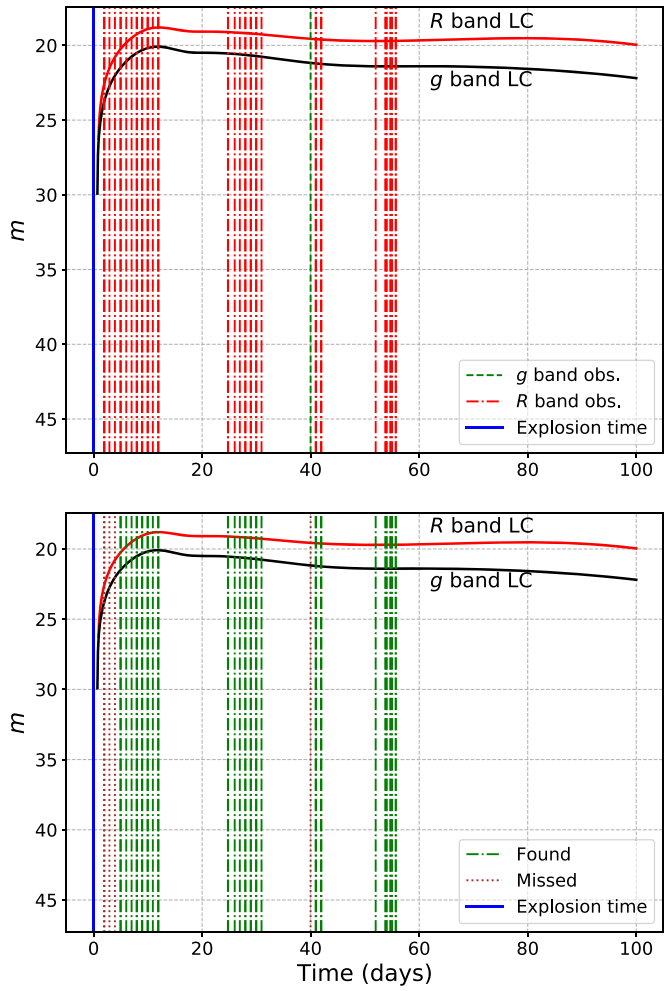

Figure 8. Upper panel: an example of an SN IIp light curve, with the apparent magnitude, m, on the y-axis and time on x-axis. The light curve is shown in the iPTF R and g bands. The observations of the telescope are shown as vertical lines. Lower panel: the same light curve is plotted, however, the vertical lines now represent the recovery by the single-epoch classifier. One can identify the only g-band observation (around 40 days) being missed due to a fainter magnitude in the g band.

galaxies in iPTF and an $E(B-V)$ extinction value from IIp extinction distribution in Hatano et al. (1998). In this case, we use the criteria that the light curve must be recovered a minimum of five epochs, brighter than the 20th magnitude in a span of 3 weeks within the 100 days postexplosion. The iPTF observing schedule along with the single-epoch classifier is used to compute the detectability in each epoch. We obtain the result

$$\langle VT \rangle_{\rm IIp} = (7.80 \pm 0.76) \times 10^{-4}\,{\rm Gpc}^3\,{\rm yr}, \qquad (11)$$

where the error includes the statistical error from the Monte Carlo integration and the 6% systematic uncertainty from the single-epoch classifier (see Section 4.2). The median sensitive redshift is found to be $z_{\rm median}^{\rm IIp} = 0.038$.

6. Discussion and Conclusions

In this work, we provide a methodology to assess the transient detectability taking into account the intrinsic transient properties and the observing conditions of fast-cadence transient surveys. This is done by injecting fake point-source transients into the images, running image subtraction on them,

and finding out the parameter space where they are found by the image subtraction pipeline. The joint detectability is evaluated using the machinery of supervised machine learning trained on the missed and found fake transients. This step mimics the action of the image subtraction pipeline at every epoch and forms the single-epoch detectability. Consequently, the light-curve morphology and the survey observing schedule are used to compute the spacetime volume sensitivity of particular transients. We consider the case of the iPTF and evaluate the single-epoch detectability and then use its observing schedule to compute the spacetime volume sensitivity of type Ia supernovae (SNe Ia). We also do a preliminary analysis of type IIp supernovae (SNe IIp). Note that the spacetime volume sensitivity could be computed for any general transient, using its light-curve morphology; SN Ia or IIp is an example. In the case of SNe Ia, the remaining piece in the estimation of the volumetric rate is a systematic number count to be obtained via an archival search into iPTF data. While we defer this to a future work, we outline our plan of action here.

6.1. Rates

The computation of the rate posterior assumes the likelihood of observing N candidate events is an inhomogeneous Poisson process (Loredo & Wasserman 1995; Farr et al. 2015). Our *search* will filter the SN Ia population based on the model presented in Section 5 at the expense of some contamination from other transient types, potentially with similar light-curve morphologies. If the mean count of these impurities is Λ_0, the likelihood function is

$$p(N|\Lambda_0, \Lambda_{\rm SNe}) \propto (\Lambda_0 p_0 + \Lambda_{\rm SNe} p_{\rm SNe})^N \times \exp(-\Lambda_0 - \Lambda_{\rm SNe}), \quad (12)$$

where $p_{\rm SNe}$ (p_0) is the a priori weight that a transient is (is not) an SN Ia after the filtering process. With a suitable choice of prior, we can use Bayes's theorem to obtain the posterior. Considering the Jeffreys's prior,

$$p(\Lambda_0, \Lambda_{\rm SNe}) = \frac{1}{\sqrt{\Lambda_0}} \frac{1}{\sqrt{\Lambda_{\rm SNe}}}, \quad (13)$$

the posterior takes the form

$$p(\Lambda_0, \Lambda_{\rm SNe}|\, N) \propto p(N|\Lambda_0, \Lambda_{\rm SNe}) p(\Lambda_0, \Lambda_{\rm SNe}) \propto \frac{(\Lambda_0 p_0 + \Lambda_{\rm SNe} p_{\rm SNe})^N}{\sqrt{\Lambda_0 \Lambda_{\rm SNe}}} \times \exp(-\Lambda_0 - \Lambda_{\rm SNe}). \quad (14)$$

Integrating out the nuisance parameter, Λ_0, we have the marginalized posterior on $\Lambda_{\rm SNe} = R\langle VT\rangle$ or, equivalently, on R:

$$p(R|N) = \int_0^\infty p(\Lambda_0, \Lambda_{\rm SNe}|\, N) d\Lambda_0 \propto \frac{e^{-R\langle VT\rangle}}{\sqrt{R\langle VT\rangle}} \times \left[(R\langle VT\rangle p_{\rm SNe})^N + \frac{N}{2} p_0 (R\langle VT\rangle p_{\rm SNe})^{N-1}\right], \quad (15)$$

where we expand Equation (14) and integrate, keeping terms up to linear order in p_0 since we expect that $p_0 \ll p_{\rm SNe}$.

6.2. Approximate SN Ia Count in iPTF

SN Ia rates have been studied earlier in the literature (Gal-Yam et al. 2007; Dilday et al. 2008; Brown et al. 2019). Deep field instruments have provided estimates of the Ia rate out to high redshift (Gal-Yam et al. 2007). The iPTF, being an all-sky survey has a comparatively lower sensitivity to SNe Ia at $z^{\rm Ia}_{\rm median} = 0.099$, evaluated in Section 5. The SDSS-II supernova survey has estimated the volumetric SN Ia rate at $z \approx 0.1$ to be $R^{\rm SDSS\text{-}II}_{\rm SNIa} \sim 2.9^{+1.07}_{-0.75} \times 10^{-5}\,{\rm Mpc}^{-3}\,{\rm yr}^{-1}$ (Dilday et al. 2008). Using our estimate of the spacetime sensitive volume from Equation (10), an estimate of the count of SNe Ia in iPTF is 630–1160. This is consistent with 1035 objects tagged "SN Ia" during the survey time.

6.3. Future Work

While the number of transients tagged as "SN Ia" by human scanners during the iPTF survey time seem consistent with our ballpark above, the systematic uncertainty of such a classification remains unquantified. The quantities p_0, $p_{\rm SNe}$, and N in Equation (15) require a systematic search into the iPTF archival data to retrieve the candidate count and systematic errors associated with such a classification. We defer this and the computation of SN Ia volumetric rate to a future work in the series.

The methodology developed here facilitates the computation of spacetime volume sensitivities of general transient types. Of particular interest are the fast transients in iPTF archival data as discussed in Ho et al. (2018). Also, the observation of the "kilonova" resulting from the binary neutron star merger, GW170817 (Abbott et al. 2017a, 2017b, 2017c), hints toward the association of transients to binary neutron star mergers. There is no evidence of detection of such a transient in the iPTF data, in which case rate upper limits could be placed due to nondetection.

This work was supported by Global Relay of Observatories Watching Transients Happen (GROWTH) project under the National Science Foundation (NSF) grant No. 1545949. The research used resources of the National Energy Research Scientific Computing Center (NERSC), a DOE Office of Science User Facility supported by the Office of Science of the U.S. Department of Energy under Contract No. DE-AC02-05CH11231. D.C. acknowledges the use of computing facilities provided by NERSC and by Leonard E. Parker Center for Gravitation, Cosmology and Astrophysics at University of Wisconsin–Milwaukee. The latter is supported by NSF Awards PHY-1626190 and PHY-1607585. P.E.N. acknowledges support from the DOE through DE-FOA-0001088, Analytical Modeling for Extreme-Scale Computing Environments. D.C. would like to thank Shaon Ghosh, Jolien Creighton, Siddharth Mohite, Angela Van Sistine, and Lin Yan for helpful discussions. We thank the anonymous referee for helpful comments.

Software: SExtractor (Bertin & Arnouts 1996), HOTPANTS (Becker 2015), Astropy (Astropy Collaboration et al. 2018), sncosmo (Barbary 2014), scikit-learn (Pedregosa et al. 2011), Matplotlib (Hunter 2007), scipy (Jones et al. 2001), numpy (van der Walt et al. 2011), pandas (McKinney 2010), jupyter (https://jupyter.org/), SQLAlchemy (https://www.sqlalchemy.org/).

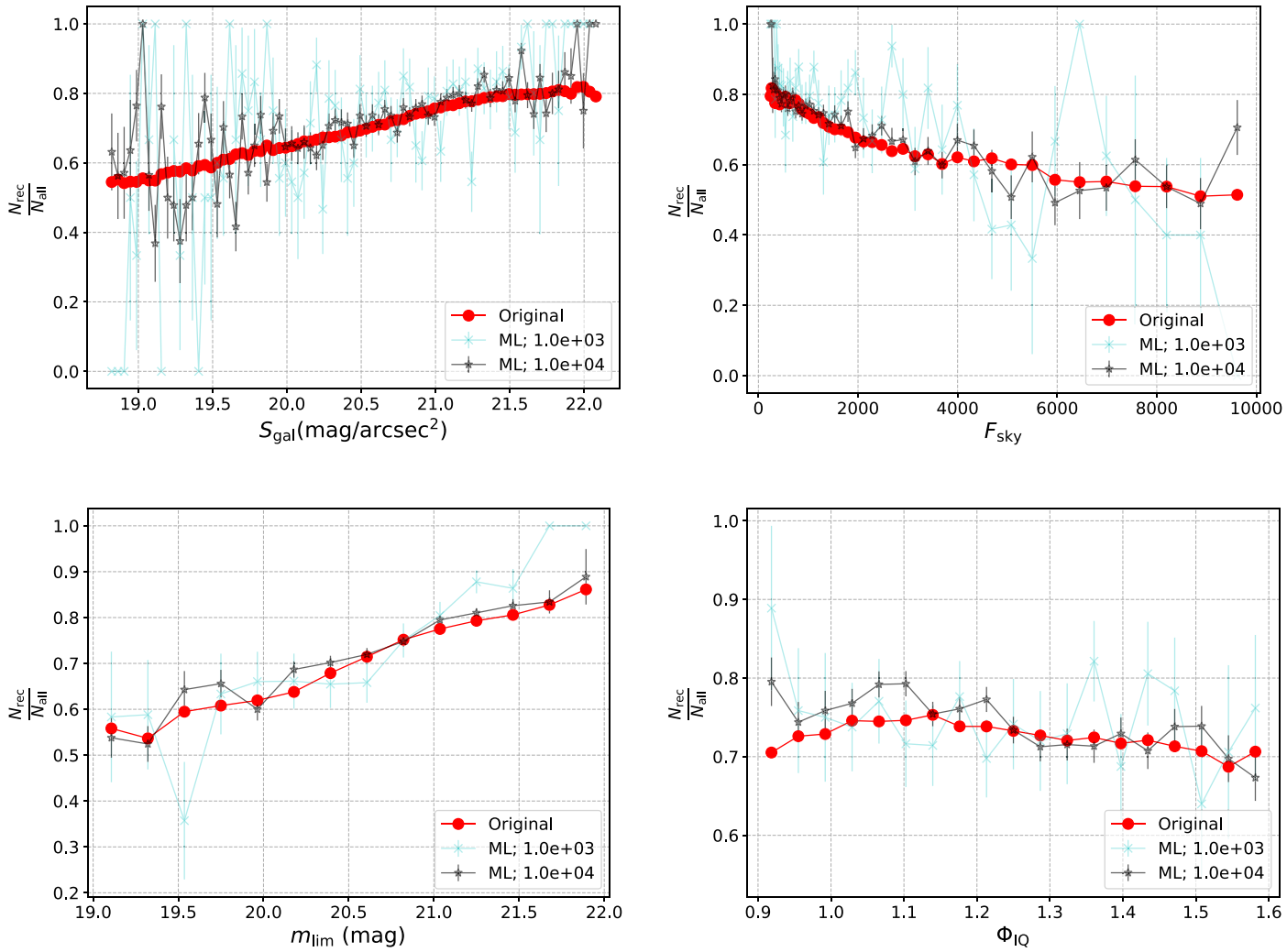

Figure 9. This figure is an extension of Figure 4. We compare the performance of the marginalized single-parameter efficiency of the trained classifier compared to that of the original distributions in Figure 3. We see the behavior of the ISP being reproduced by feeding the classifier a few thousand points.

Appendix
Classifier Single-epoch Performance

In Figure 4, we made a comparison between the marginalized single-parameter efficiency for the single-epoch transient brightness from the classifier predictions. Here, we show it for the remaining parameters. While the final classifier is trained on the full data set, to make the comparison, we train it on 90% of the total fake point-source simulations we performed, as mentioned in Section 3.1. From the remaining 10% sample size, we make a random selection of points (progressively increasing), feed them to the classifier, and bin the results in the same manner as in Figure 3 to compare marginalized efficiency plots. These are shown in Figure 9 and Figure 4, the latter presented in the main text. We see that the behavior starts to converge to that of the ISP in a few thousand points.

ORCID iDs

Deep Chatterjee https://orcid.org/0000-0003-0038-5468
Peter E. Nugent https://orcid.org/0000-0002-3389-0586
David L. Kaplan https://orcid.org/0000-0001-6295-2881
Mansi M. Kasliwal https://orcid.org/0000-0002-5619-4938

References

Abbott, B. P., Abbott, R., Abbott, T. D., et al. 2017a, ApJL, 848, L12
Abbott, B. P., Abbott, R., Abbott, T. D., et al. 2017b, ApJL, 850, L39
Abbott, B. P., Abbott, R., Abbott, T. D., et al. 2017c, ApJL, 848, L13
Astropy Collaboration, Price-Whelan, A. M., Sipőcz, B. M., et al. 2018, AJ, 156, 123
Barbary, K. 2014, Zenodo, doi:10.5281/zenodo.11938
Becker, A. 2015, Astrophysics Source Code Library, ascl:1504.004
Bertin, E., & Arnouts, S. 1996, A&AS, 117, 393
Betoule, M., Kessler, R., Guy, J., et al. 2014, A&A, 568, A22
Bloom, J. S., Brink, H., Richards, J. W., et al. 2013, MNRAS, 435, 1047
Brown, J. S., Kochanek, C. S., Stanek, K. Z., et al. 2019, MNRAS, 484, 3785
Cao, Y., Nugent, P. E., & Kasliwal, M. M. 2016, PASP, 128, 114502
Dilday, B., Kessler, R., Frieman, J. A., et al. 2008, ApJ, 682, 262
Drake, A. J., Djorgovski, S. G., Mahabal, A., et al. 2009, ApJ, 696, 870
Farr, W. M., Gair, J. R., Mandel, I., & Cutler, C. 2015, PhRvD, 91, 023005
Fitzpatrick, E. L. 1999, PASP, 111, 63
Frohmaier, C., Sullivan, M., Maguire, K., & Nugent, P. 2018, ApJ, 858, 50
Frohmaier, C., Sullivan, M., Nugent, P. E., Goldstein, D. A., & DeRose, J. 2017, ApJS, 230, 4
Gal-Yam, A., Filippenko, A. V., Jannuzi, B. T., et al. 2007, MNRAS, 382, 1169
Gilliland, R. L., Nugent, P. E., & Phillips, M. M. 1999, ApJ, 521, 30
Guy, J., Astier, P., Baumont, S., et al. 2007, A&A, 466, 11
Hatano, K., Branch, D., & Deaton, J. 1998, ApJ, 502, 177
Hinshaw, G., Larson, D., Komatsu, E., et al. 2013, ApJS, 208, 19

Ho, A. Y. Q., Kulkarni, S. R., Nugent, P. E., et al. 2018, ApJL, 854, L13
Holoien, T. W.-S., Brown, J. S., Vallely, P. J., et al. 2019, MNRAS, 484, 1899
Hunter, J. D. 2007, CSE, 9, 90
Ivezić, Ž, Kahn, S. M., Tyson, J. A., et al. 2019, ApJ, 873, 111
Jones, E., Oliphant, T., Peterson, P., et al. 2001, SciPy: Open source scientific tools for Python
Kaiser, N., Burgett, W., Chambers, K., et al. 2010, Proc. SPIE, 7733, 77330E
Kulkarni, S. R. 2016, AAS Meeting Abstracts, 227, 314.01
Law, N. M., Kulkarni, S. R., Dekany, R. G., et al. 2009, PASP, 121, 1395
Li, W., Chornock, R., Leaman, J., et al. 2011, MNRAS, 412, 1473
Loredo, T. J., & Wasserman, I. M. 1995, ApJS, 96, 261
Maoz, D., & Mannucci, F. 2012, PASA, 29, 447
McKinney, W. 2010, in Proc. 9th Python in Science Conf., Data structures for statistical computing in Python, ed. S. van der Walt & J. Millman, 51
Nugent, P., Cao, Y., & Kasliwal, M. 2015, Proc. SPIE, 128, 114502
Pedregosa, F., Varoquaux, G., Gramfort, A., et al. 2011, Journal of Machine Learning Research, 12, 2825
Richardson, D., Jenkins, R. L. I., Wright, J., & Maddox, L. 2014, AJ, 147, 118
Sako, M., Bassett, B., Becker, A., et al. 2007, AJ, 135, 348
Shanks, T., Metcalfe, N., Chehade, B., et al. 2015, MNRAS, 451, 4238
van der Walt, S., Colbert, S. C., & Varoquaux, G. 2011, CSE, 13, 22